Composite Structures 296 (2022) 115887

Contents lists available at ScienceDirect

Composite Structures

journal homepage: www.elsevier.com/locate/compstruct

Testing and simulation of a composite-aluminium wingbox subcomponent subjected to thermal loading

José M. Guerrero *, Aravind Sasikumar, Jordi Llobet, Josep Costa

AMADE, Polytechnic School, Universitat de Girona, Campus Montilivi s/n, E-17003 Girona, Spain

ARTICLE INFO

Keywords:
Bolted joints
Testing
Thermal loading
Aircraft structure
Composite laminates
Finite element method

ABSTRACT

Modern aircraft designs combine carbon–aluminium assemblies mechanically joined by steel bolts. The different thermal expansion coefficient of these materials and the substantial temperature excursions during aircraft operation, lead to thermal stresses that alter the load distribution of the bolted joint. These stresses can compromise the structural integrity of large components and they are difficult to anticipate. In this paper, we present a detailed experimental and computational study of a hybrid carbon–aluminium wingbox subcomponent. Thermal tests were performed to determine the global deformation of the assembly. The numerical model is compared against the experiments and is used to extract additional information that cannot be easily measured experimentally, for instance the evolution of the bolt preload with temperature. The agreement between the experimental results and simulation instils confidence in the proposed methodology to identify, and minimise through redesign, areas prone to damage due to the combination of thermal and mechanical loads.

1. Introduction

Nowadays, Carbon Fibre Reinforced Polymers (CFRP) are increasingly being used to replace metallic parts in aircraft components, thanks to their reduced weight-to-strength ratio. That said, metallic elements (mainly aluminium and titanium) are still being employed, which has led to the presence of several metal–CFRP assemblies in the wings, empennage or fuselage [1,2]. Due to their high stiffness and strength as well as their facility to be disassembled and repaired, bolted joints are widely used for connecting these types of assemblies [3,4]. At cruising altitudes, an aircraft experiences temperatures between −30 °C to −50 °C, but during the landing phase the temperatures range between 40 °C to 50 °C. Given that metals and CFRP have different thermal expansion coefficients, these substantial jumps in temperature cause thermal stresses which affect the performance of the bolted joints [5–7]. At the same time, detailed designing and analysing large bolted components of complex geometry is challenging due to the complex phenomenology involved, which includes not only the differential thermal expansion, but also bolt preload, bolt-hole clearance and friction and sliding between the contacting surfaces [3,4,6–11].

Aircraft manufacturers are already concerned by safety problems caused by thermal fatigue of the primary structures with hybrid materials. For example, the Airbus A380 combines CFRP with aluminium ribs in its wings. After years of service, cracks were found during an inspection that had originated from the rib-to-skin panel attachment joint. Further cracks were also observed at the web of the rib feet [2,12]. These cracks were attributed to high stresses in the joints due the thermal expansion mismatch between the parts [2,13]. Thus, the design of the ribs is crucial to avoid high stresses that originate at the central lightning holes and also at the mouse holes (a curved region of the rib that leaves a gap between the rib bay and the skin/spar sections as shown in Fig. 1). In these locations, thermal-induced stresses can be high enough to trigger a fatigue crack. Moreover, unfolding, which refers to the fact that the angle between the rib-skin, and between the rib-spar deviates from 90°, can also occur. This issue of the unfolding of the rib is also relevant since it changes the shape of rib and the way the load is distributed on the three elements: rib, skin and spar.

Currently, aerospace industry design philosophy consists of verifying the static and fatigue strength by experimental testing, following the classical pyramidal approach [1,14]. Firstly, at the coupon level, several specimens are tested to understand the main physics of the problem [15]. Secondly, a substructure representative of the real structure is tested and, finally, the full real structure is analysed. Unfortunately, testing at the substructural and structural levels is challenging and costly due to: (i) the need for complex and expensive testing equipment, (ii) the large amount of data to be measured and processed, (iii) the high manufacturing and instrumentation costs and (iv) the difficulty in knowing beforehand which critical areas from the structure need to be instrumented. In addition, at any of these levels, the thermal

* Corresponding author.
E-mail address: josemanuel.guerrero@udg.edu (J.M. Guerrero).

https://doi.org/10.1016/j.compstruct.2022.115887
Received 21 January 2022; Received in revised form 27 May 2022; Accepted 12 June 2022
Available online 18 June 2022

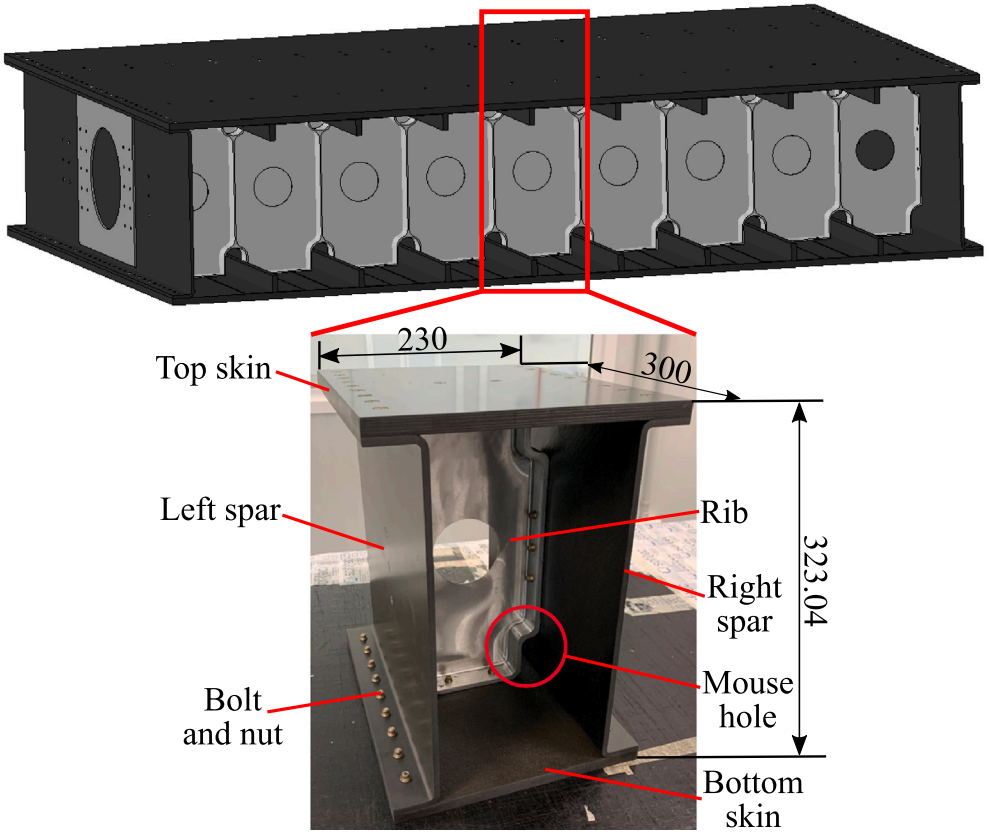

Fig. 1. Photo of the manufactured wingbox subcomponent representing a small unit of a full wingbox.

strain needs to be taken into account since it may affect the global response, thus adding a further complexity to the tests [1,2,7]. Finally, thermal tests performed with materials that exhibit low Coefficient of Thermal Expansion (CTE) values, like composites, result in small deformation levels that are difficult to measure.

From a computational point of view, several refined Finite Element (FE) models able to capture the phenomenology involved in bolted joints (contact, friction, sliding, transverse stresses, bolt preload, clearance and thermal expansion/contraction) with high-fidelity have been extensively presented in the literature [3,7,16–25]. Nonetheless, such refined models are computationally demanding, therefore limiting their applicability to designing and analysing large structures [3,7,25,26]. Recently, Guerrero et al. [7] presented a simplified FE model where the plates are modelled with solid-shell elements (i.e. a continuum shell), whereas the bolt is simulated with a beam and surface elements. The model was validated, on both the coupon and substructural scales, by comparing it with a full 3D solid model showing an excellent trade-off between computational time and accuracy. Nevertheless, the model was not compared with experimental data.

In this paper, we propose a representative carbon–aluminium hybrid subcomponent of a wingbox and experimentally subject it to positive and negative thermal excursions, representing the typical thermal cycles aircraft experience during their service life. Detailed instrumentation plans along with accurate strain measurements from hybrid material structures are proposed. The numerical model proposed by Guerrero et al. [7] is used to simulate the subcomponent and is validated against the experimental data. Using the experimental results, also complemented by the numerical results, we analyse the global thermal deformation of the subcomponent and also study the effect of the thermal excursions on the specific concerns raised by the aeronautical manufacturers, i.e., unfolding, hoop stresses in the rib, etc. Our results show a significant presence of unfolding and considerable stresses in the assembly due to the thermal loads, which can then lead to structural concerns. The good agreement between the experimental and numerical results instils confidence in the proposed methodology to identify the most critical areas and provide insights into the design of a new rib with lower thermal-induced stresses and improved thermal response. This paper aims to validate the experimental methodology and to verify the accuracy of the numerical model proposed in Guerrero et al. [7]. The authors also plan to use the same strategy to study the thermal behaviour of a full-scale wingbox assembly in a future paper. This work is part of an EU Cleansky-2 project 'INNOHYBOX', developed within the consortium of Dassault Aviation, the AMADE research group from the University of Girona, the technological centre EURECAT and the company SOFITEC, with the global objective of analysing a hybrid wingbox structure subjected to thermo-mechanical loads.

2. Methodology

In this section we describe the wingbox subcomponent assembly, the experimental testing campaign carried out and the finite element model developed.

2.1. Wingbox subcomponent description

The wingbox subcomponent consists of a small representative unit of a full wingbox cross-section, see Fig. 1. The subcomponent is comprised of three parts: the skin (top and bottom) and spar (left and right), both made of CFRP, and one rib bay at the centre made of aluminium. All these parts are bolted together with NAS-1153 steel bolts, as follows:

- Top and bottom skin are bolted with the rib by 2 bolts each.
- Left and right spars are bolted with the rib by 3 bolts each.
- Skins and spars are bolted together by 36 bolts in total.

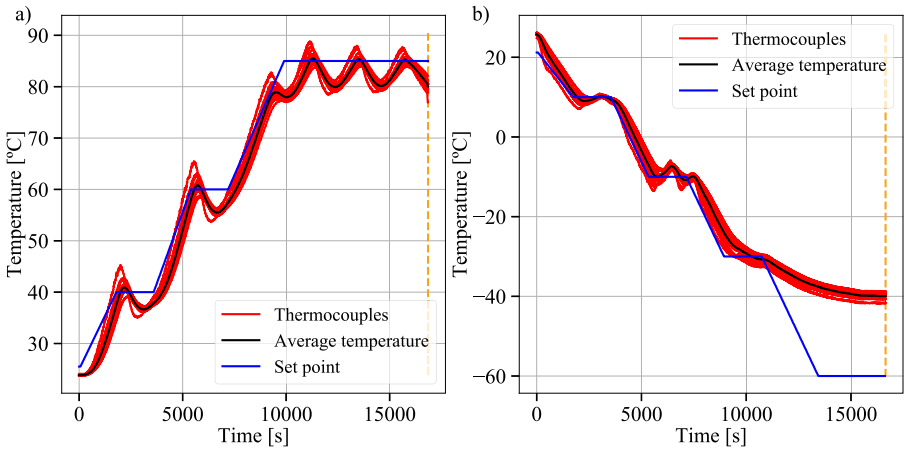

Fig. 2. Temperature ramps conducted for the experimental tests of the subcomponent. (a) Positive thermal and (b) negative thermal. The dashed vertical line indicates the time at which the experimental data is compared with the numerical model. The set point indicates the temperature set in the heating/cooling machine.

Hence, the assembly contains 46 bolts, see Fig. 1. The torque applied to the bolts was approximately 3.4 N m, (corresponding to a theoretical preload of around 6000 N), which is a common torque used in aerospace.

The subcomponent has been downsized to a ratio of 6.5 with respect to the wingbox, but has mainly the same key elements to perform a preliminary analysis, thereby, reducing the complexity and experimental cost. The downsized model was designed in such a way that it focused on studying a single rib bay and the interaction between the bolted joints of different materials. Therefore, the subcomponent will allow the study of the thermal response in a simpler structure, observing critical areas of design concern such as the central hole of the rib, the mouse hole and the presence of unfolding, see Fig. 1. The dimensions of the subcomponent are $230 \times 300 \times 323.04$ mm (width × length × height). Other specific dimensions such as the thickness, radius of the parts, etc., are confidential. Notice that we removed the stringers in the skin, since their behaviour was out of interest at this scale.

2.2. Experimental tests

To represent the temperature excursions seen on an aircraft during its operational service life, the subcomponent is subjected to a thermal jump. Two tests were performed:

- Negative thermal jump: from room temperature (25 °C) down to −40 °C.
- Positive thermal jump: from room temperature (25 °C) up to 80 °C.

For each test, the subcomponent was placed inside a climatic chamber at room temperature. To ensure a uniform temperature over the whole assembly and to avoid oscillations resulting from the thermal inertia of the components, the thermal jump was slowly applied through small temperature ramps over long periods of time. A total of 16 thermocouples were bonded at different locations of the subcomponent so as to map the temperature during the thermal cycle. Fig. 2 shows the evolution of the temperature signal measured by the different thermocouples, the calculated average temperature and the temperature sensor that controlled the thermal unit. For the positive thermal test, the average temperature shows some oscillations of 5 °C with respect to the control temperature set at 85 °C at the end of the test. For the negative thermal test, the control temperature was set at −60 °C but the assembly stabilised at −40 °C, thus reaching its maximum cooling capacity. The dashed lines in Fig. 2 mark the end of the thermal tests.

The subcomponent was placed inside the chamber and supported by an aluminium frame at four corners of the bottom skin, thus allowing free expansion/contraction during the thermal jump (see Fig. 3). An insulation tape was used at the supports to avoid heat transfer by conduction via the aluminium frame. Besides this, strain gauges were bonded onto the assembly to track the strains at different key locations; as will be explained next. A photo of the subcomponent just before and after the negative thermal test is also presented in Fig. 3.

2.3. Experimental instrumentation

Self-temperature-compensated strain gauges from HBM were selected to monitor the strain field at the subcomponent. As a general rule, it is good practice to use self-temperature compensated gauges with a similar CTE to the material under study. A 350 Ohms gauge is also preferable to minimise self-heating by the excitation current. In addition, a medium gauge length is recommended to improve heat transfer over to the substrate. In this case, two different types of 6 mm length gauges were used: one aluminium strain gauge with temperature compensation with CTE = 23 μm/m°C (1-LY63-6/350) was used for the aluminium rib, while another with a lower thermal expansion like quartz, with CTE = 0.5 μm/m°C, was employed for the CFRP laminates (1-LY46-6/350). Each strain gauge was connected via a four-wire quarter-bridge circuit to compensate the resistance change of the cables, as is recommended by HBM.

Recall that the electrical resistance of the strain gauge changes not only with mechanical strain, but with temperature as well. In addition, the gauge factor, which relates the strain and the gauge resistance change, also varies with temperature. These deviations can cause significant errors if not properly accounted for. The strain measurement, due to a purely temperature change, is commonly referred to as the 'thermal output' or 'apparent strain' of the strain gauge. This thermal output is caused by two effects. First, the electrical resistivity of the grid conductor is temperature dependent and so is the gauge resistance. The second contribution is the CTE mismatch between the grid and the test part (or substrate) where the strain gauge is bonded [27,28]. Consequently, the strain that is measured by the strain indicator, ε_{ind}, during the thermal test is given by

$$\varepsilon_{\text{ind}} = \varepsilon_{\text{m}} + \varepsilon_{\text{p}} + \left(\alpha_{\text{c}} - \alpha_{\text{g}}\right) \Delta T = \varepsilon_{\text{m}} + \varepsilon_{\text{p}} + \alpha_{\text{c}} \Delta T - \alpha_{\text{g}} \Delta T \tag{1}$$

where ε_{m} is the mechanical strain (all the strain that is related to the stress), ε_{p} is the strain due to the resistance change, which can be computed with a polynomial equation from the strain gauge datasheet, α_{c} is the CTE of the specimen, α_{g} is the CTE of the grid (indicated in the datasheet) and ΔT is the thermal jump. Notice that if $\alpha_{\text{c}} = \alpha_{\text{g}}$, there is no thermal mismatch between the grid and substrate and hence, the last term in Eq. (1) vanishes. It should be noted the self-temperature-compensated strain gauges are processed to minimise the thermal output compared to standard foil gauges. Table 1 shows the properties of the strain gauges employed for the tests.

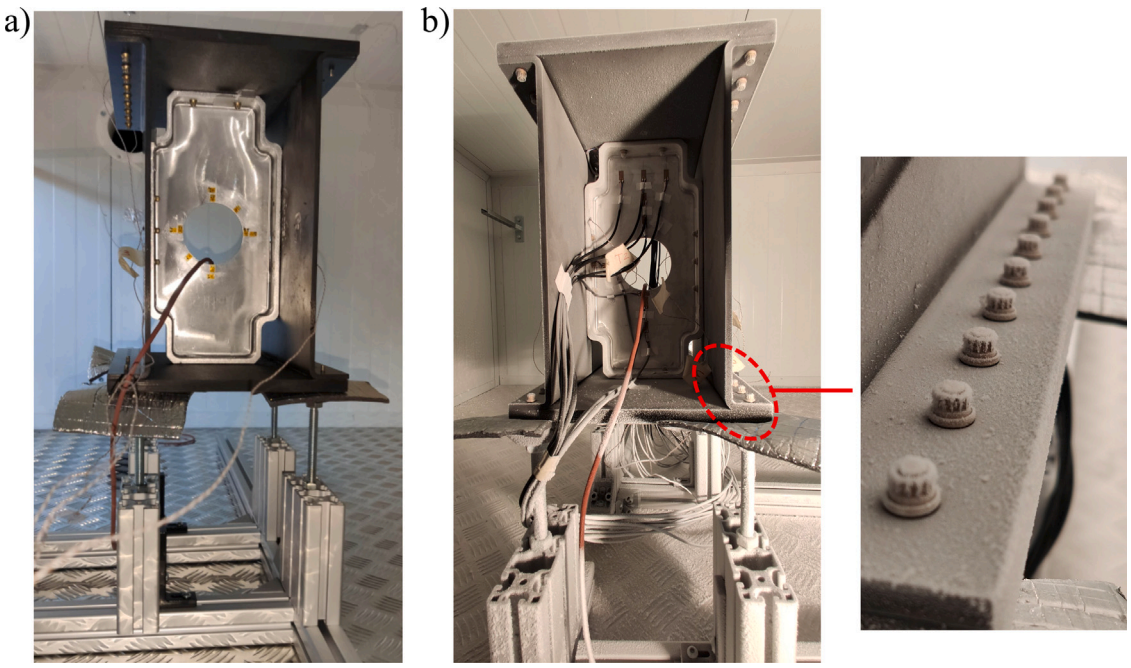

Fig. 3. (a) Subcomponent placed inside the thermal chamber before testing and (b) subcomponent just after the negative thermal test, showing the presence of frost created during the low temperature. The assembly is supported at each of the four corners by an aluminium structure. Some strain gauges are also illustrated.

Table 1
Properties of the strain gauges used for the experimental tests.

Strain gauge reference	Material type	α_g [μm/m°C]	ε_p [μm/m]
1-LY63-6/350	Aluminium	23	$-12.11 + 1.29 \cdot T - 3.91 \cdot 10^{-2} \cdot T^2 + 2.10 \cdot 10^{-4} \cdot T^3 \pm (T - 20) \cdot 0.3$
1-LY46-6/350	Quartz	0.5	$-16.40 + 2.39 \cdot T - 8.60 \cdot 10^{-2} \cdot T^2 + 3.45 \cdot 10^{-4} \cdot T^3 \pm (T - 20) \cdot 0.3$

In this work, we compute the 'total strain' (ε_t), which we refer as the mechanical strain, ε_m (stress-induced strain, i.e. all the strain that causes stress), plus the strain due to the thermal expansion of the specimen $(\alpha_c \Delta T)$, so that $\varepsilon_t = \varepsilon_m + \alpha_c \Delta T$. Hence, to obtain the total strain from the experimental measurements, the measured experimental strains are corrected simply by re-organising Eq. (1), leading to

$$\varepsilon_t = \varepsilon_m + \alpha_c \Delta T = \varepsilon_{ind} - \varepsilon_p + \alpha_g \Delta T \tag{2}$$

In Eq. (2), ε_{ind} is known since this corresponds to the strain gauge signal measured during the test, while ε_p and α_g are known from the strain gauge datasheet (Table 1). It is worth mentioning that Eq. (2) assumes the CTE of the coupon and grid do not change with temperature, which is a valid assumption for the range of temperatures used in this work. The variation of the gauge factor with the current temperature range can be neglected.

The validity of Eq. (2) was confirmed as follows. An aluminium coupon, with two longitudinal aluminium strain gauges bonded, and a CFRP coupon, with four quartz strain gauges bonded (two longitudinally and two transversally), were subjected to a pure thermal cycle. The strain given by the indicator was corrected with Eq. (2). Since the mechanical strain was zero (i.e. the coupons expanded/contracted freely, so that $\varepsilon_m = 0$), the total strain computed from Eq. (2), ε_t, equals $\alpha_c \Delta T$. Hence, we can perform a least square linear fitting of the experimental data, in which the slope is the CTE of the coupon (α_c). In the case of aluminium, we obtained a CTE of 23.05 μm/m°C, which agrees well with the aluminium alloy used, see Fig. 4a. For the CFRP we obtained a CTE between 0.2219 and 0.4072 μm/m°C longitudinally, while in the transverse direction we estimated a CTE between 4.58 and 4.88 μm/m°C. This agrees well with the CTE of 0.29 ± 0.25 and 4.92 ± 1.5 in the longitudinal and transverse directions, respectively, that were determined using a push-rod dilatometer test according to ASTM E228-11 [29], see Fig. 4b–c. The agreement between the result from Eq. (2) and the expected CTE proves the validity of the strain correction approach. It is worth noting that some strain oscillations appear in Fig. 4, this is because the temperature change was applied in ramps that were too short, but this does not affect the validation of the results.

It is also worth mentioning that other tests were also performed by bonding steel strain gauges onto the same aluminium and CFRP coupons. The results indicated that the strain correction provided by Eq. (2) worked well in the aluminium material, but it was not accurate with the CFRP. Consequently, Eq. (2) cannot be used directly if the mismatch between the CTE of the material tested and the grid is considerable.

A total of 32 strain gauges were placed at different locations of the rib, top skin and left spar in order to track the 3D global deformation of the assembly, see Fig. 3. In the skin and spar, strain gauges were placed along the parts with the objective of measuring the direction of the bending of the components, so that the deformation in the experiments could be compared with the numerical model. Moreover, the aim was also to compare the absolute strain values at these different places to check that, the numerical model was not only capturing the same deformation as in the experiments, but also similar strain magnitudes. On the other hand, in the rib we placed strain gauges in locations that are of interest for the industry: around the central hole (to understand the deformation in such critical area and measure the hoop stresses), as well as around the top region of the rib, with the objective of measuring unfolding. Unfortunately, we were unable to place strain gauges in the mouse hole. The exact location of all strain gauges will be shown in Section 3.

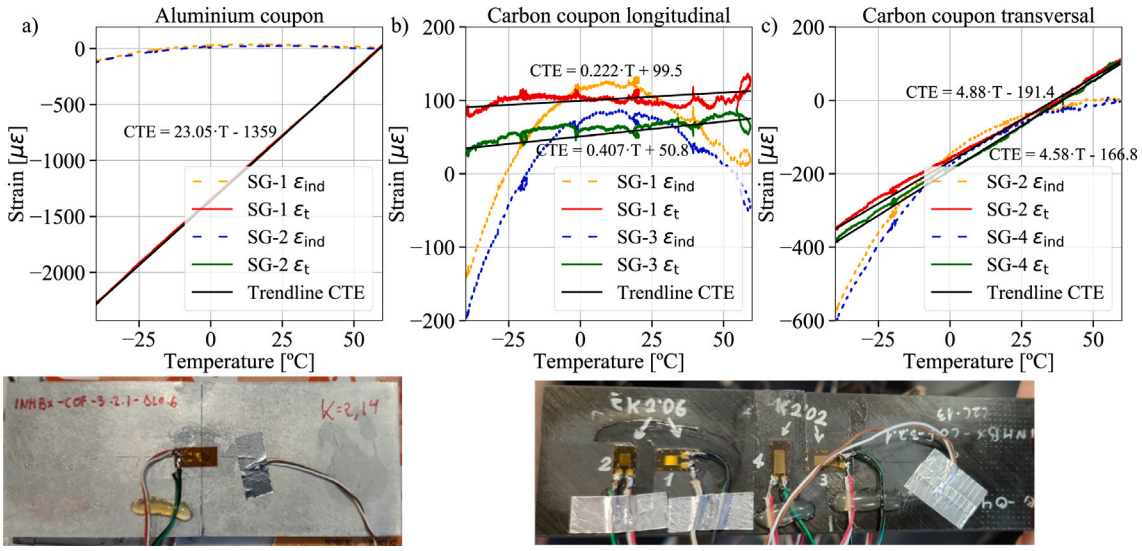

Fig. 4. Measured strain, ε_{ind}, and corrected total strain, ε_t, for the aluminium and CFRP coupons. (a) Aluminium, (b) CFRP longitudinal and (c) CFRP transversal. The slope of the trendline corresponds to the CTE of the specimen, which agrees well with the theoretical one. Photos of the specimens are also shown.

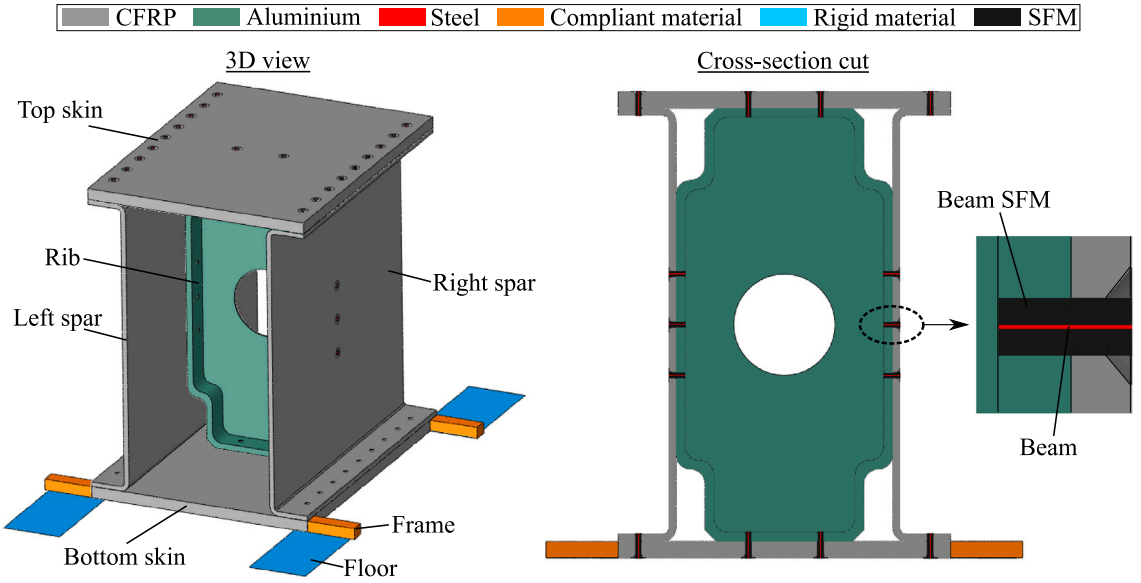

Fig. 5. Finite element model of the wingbox subcomponent, based on continuum shells to model the parts, while beams and surface elements (SFM) are employed to represent the bolts.

2.4. Subcomponent finite element model

The subcomponent FE model is the same as that described in Guerrero et al. [7], although some small changes were performed. The simulation was carried out using the Abaqus 6.14 finite element programme [30], following an implicit static analysis. All the components of the structure (skins, spars and rib) are modelled as type SC8R Continuum Shells (CONTS) (i.e. an eight node quadrilateral continuum element with reduced integration). These elements have only displacement degrees of freedom and look like solid elements, but their kinematic formulation mimics that of conventional shells being, therefore, in-between solid and shell elements [7]. Unlike conventional shells, continuum shells can partially capture the through-thickness behaviour, albeit their response is simplified compared with solids [7,30]. Fig. 5 presents a global picture of the FE model. All the geometry and dimensions mirror the real assembly. Frames and floors are included for applying boundary conditions representative of the real test, as will be clarified later.

The bolts are modelled with type B31 beam elements (a two node linear beam). The bolt section was simplified from a countersunk shape to fully cylindrical, with a diameter equal to that of the bolt thread all along its length [7]. Given that beam elements do not have a physical cross-section (i.e. only a line is physically modelled with a virtual cross-section), a cylindrical surface with a diameter equal to that of the bolt is included to physically represent its outer surface, see Figs. 5 and 6a. This surface is meshed with Surface Elements (SFM) of type SFM3D4R (four node quadrilateral surface element with reduced integration). The SFM is connected with its beam by a tie constraint, where the beam is selected as the master and the SFM as the slave [7], see Fig. 6a. Consequently, the SFM can be seen as a lattice of nodes, without stiffness and material properties, whose motion is governed following the displacements and rotations of the beam, without storing elastic energy [7,30].

To further simplify the physics, the washer and nut are not physically modelled [7]. Instead, their presence is partially represented as follows. First, a circular partition with diameter equal to that of the

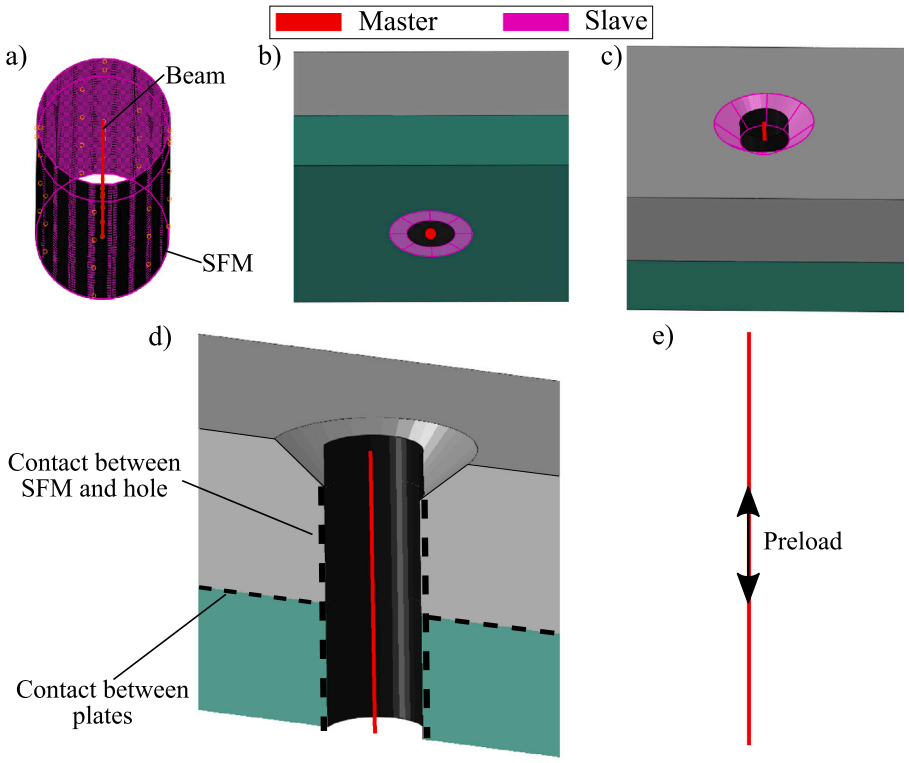

Fig. 6. Schema of the bolted joint physics. (a) Bolt modelled as beam and surface elements (SFM), with both being tied, (b) Tie between the bottom node of the beam and the washer partition, (c) Tie between the top nodes of the beam and the countersunk surface, (d) Contacts of the joint and (e) Preload assigned to the beam.

washer is created in the bottom plate of the joint, where the washer would be in contact. The bottom node of the beam (as the master) is tied with this circular partition (as the slave, see Fig. 6b). Similarly, the top nodes of the beam (as master) are tied with the countersunk surface of the top plate (as slave, Fig. 6c). Hence, the contact of the bolt head with the top plate of the joint and that of the washer with the bottom plate are neglected. Notice that, while removing the washer and nut does not greatly reduce the number of elements in the subcomponent, it simplifies significantly the problem since the contact between the washer and the assembled parts disappears. Further to this, the final aim of the authors is to use the present model to simulate a full wingbox (with around 300 bolted joints) in a future paper. In such case, the removal of the washer and nut would considerably reduce the degrees of freedom due to the very large number of bolted joints, in addition to the removal of hundreds of contact interactions. For these reasons, it was decided to remove the washer and nut.

All contact interactions, including frictional sliding, are modelled using the surface-to-surface contact algorithm of Abaqus/Standard, with the finite sliding formulation. The tangential behaviour follows a penalty friction formulation, whereas the normal behaviour is given by hard contact [7,30]. In total, we assigned contact interactions between [7]: (i) the skins and the rib, (ii) the spars and the rib, (iii) the skins and the spars, (iv) the bottom skin and the floor, (v) the frames and the floor and (vi) the SFM of the bolts and their holes. Fig. 6d shows a schematic representation of the contact in a bolted joint. The addition of the SFM was to capture the contact between the bolt and the hole. Without the SFM, this contact cannot be properly modelled since the beam does not have a physical cross-section [7]. The clearance between the holes and the bolts is 0.06 mm, which corresponds approximately to the real structure, and is within the range found in aerospace, i.e. commonly between 0.05–0.15 mm [7,9,31]. The friction coefficient for the different material interfaces, which depends on the temperature, can be found in Table 2. The values were determined from experimental testing using a newly developed device for multi-material friction testing, and will be reported in a future paper. It is worth mentioning that the subcomponent results presented in Guerrero et al. [7], used a constant friction coefficient for all the assembly. Hence, results obtained in this work are different from the ones found in [7].

Table 2
Friction coefficient for each contact interface as a function of temperature.

Contact interface	Temperature [°C]	Friction coefficient [-]
CFRP–Aluminium	−55	0.373
	25	0.315
	80	0.273
CFRP–CFRP	−55	0.161
	25	0.126
	80	0.104
Steel–CFRP or Steel–Aluminium	−55	0.315
	25	0.315
	80	0.315

The material properties are presented in Table 3. All metallic parts behave as linear elastic isotropic materials, while the CFRP components are orthotropic. The CFRP skin and spar laminates have 60 and 26 plies, respectively. The stacking sequence used for the laminates is confidential. They are defined using the 'composite layup' feature of Abaqus, which assumes classical laminate theory [30]. Three integration points are used for each ply of the laminates. The CTE is isotropic for metals and orthotropic for CFRP. Any form of damage or plasticity is ignored, since such phenomena are not expected in the real experimental test. All material properties were assumed to be independent of temperature, which is a reasonable assumption for the range of temperatures used in this study. Further to this, the weight of the assembly (about 4.62 Kg) is included by using the gravity feature of Abaqus [30], which applies a load in the gravity direction to each element of the model according to the element's material density and volume [7].

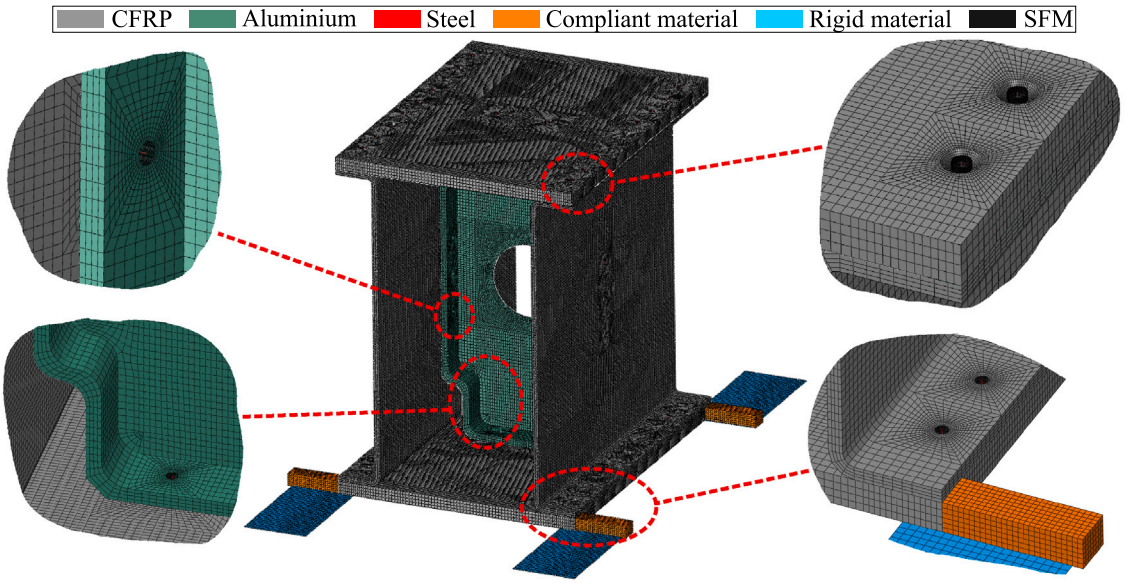

Fig. 7. Illustration of the mesh employed in the subcomponent finite element model.

Table 3
Material properties of subcomponent. (*) These properties were computed by means of experimental testing in accordance with the ASTM standards D3039M, D3518M and E228-11 [29,32,33]. CFRP properties are ply-based, with subindex 11, 22, 33 referring to the longitudinal, transverse and out-of-plane directions.

Material name	Property		Source
Steel alloy	E [MPa]	210000	[34]
	ν [-]	0.3	
	α [μm/m°C]	11	
	ρ [g/cm^3]	8	
Aluminium (2024-O)	E [MPa]	73100	[34]
	ν [-]	0.33	
	α [μm/m°C]	21	
	ρ [g/cm^3]	2.7	
CFRP (M21 EV/IMA)	E_{11} [MPa]	165000	[15]
	E_{22}&E_{33} [MPa]	9300	Own(*)
	ν_{12}&ν_{13} [-]	0.35	[15]
	ν_{23} [-]	0.487	Own(*)
	G_{12}&G_{13} [MPa]	5080	Own(*)
	G_{23} [MPa]	3127.10	$E_{22}/2\left(1+\nu_{23}\right)$
	α_{11} [μm/m°C]	-0.4 ± 0.2	Own(*)
	α_{22} [μm/m°C]	27 ± 0.5	Own(*)
	α_{33} [μm/m°C]	33 ± 2.1	Own(*)
	ρ [g/cm^3]	1.5	–
	Ply thickness [mm]	0.192	–

Overall, the mesh size is 3 mm, but this is refined to 0.5–0.75 mm around the holes to increase the stress accuracy in these areas of high stress gradients. To properly capture the bending of the parts, four elements through the thickness are used. The bolts have a mesh size of 0.3–0.5 mm. The hexahedral element mesh is structured to keep a reasonable element quality, see Fig. 7. In total, the model contains 573138 elements: 444128 hexahedral continuum shell elements, 126578 quadrilateral surface elements and 2432 beam elements. These mesh dimensions described above were selected to have an accurate representation of the geometrical features, without compromising the computational cost. The numerical model will be compared against the experiments in regions far from stress concentration.

The boundary conditions are selected to accurately represent the real experimental test (as shown in Fig. 3), and are the same as described in previous work [7]. Hence, the four corners of the subcomponent are placed just on top of four perfectly rigid surfaces, here called floors, which represent the aluminium structure where the subcomponent is supported in the experimental tests, see Fig. 3. These floors are fully clamped (Fig. 8), nonetheless, just placing the subcomponent on top of the floors does not prevent rigid body motion [7]. Consequently, we tied four fictitious 'frames', which are made of a dummy compliant material of low stiffness (0.1 GPa), at each corner of the bottom skin, see Figs. 5 and 8. Half of the frame is clamped, while the other half, that is closest to the skin, is left free (Fig. 8). Within this, the bottom skin is able to move totally freely, since no boundary conditions are applied to it, and the presence of the compliant frames prevent rigid body motion without altering the response, since their stiffness is insignificant [7]. It should be noted that we did not consider non-linear geometrical effects, since large deformation is not expected in a thermal analysis.

The simulation consists of the following two steps [7]:

- Step 1: Preload. A preload of 6000 N is given to all 46 bolts in the assembly, which corresponds to its real counterpart. This preload is applied using the bolt load feature of Abaqus [3,7,25,30], which adjusts the length of the beam's central element along the bolt axis until the sum of the reaction forces of the nodes within the element matches the user-defined preload force, see Fig. 6e. Notice that, in the next step of the simulation, the bolts are allowed to deform freely when other loads occur. Moreover, using the pre-defined field option of Abaqus [7,30], the temperature is adjusted to 25 °C (room temperature) over the whole substructure. The gravity loading is applied at the start of the step and propagated for the rest of the simulation (Fig. 8a).
- Step 2: Thermal jump. As in the experiments, the effect of a thermal jump is investigated. Either a positive, between 25 °C up to a maximum of 80 °C, or a negative jump, from 25 °C down to −40 °C are applied (Fig. 8b). To model this thermal loading, we increase or decrease the initial temperature given originally to the substructure in the previous step (25 °C) to the final temperature desired [7,30]. The different components will expand or contract according to their CTE, the stiffness of the parts, the temperature difference, and the interaction between the parts.

It is worth noting that, using other element types (such as 3D solids and conventional shell elements) was explored in previous work [7]. In this paper, we decided to use the continuum shell element because it provides excellent trade-off between computational time and accuracy of results [7]. While using beam elements to simulate bolts is commonly done in the literature [7,35], the model presents the novelty of including surface elements to capture the bearing contact of the bolt with the hole [7]. In addition, the good balance between computational

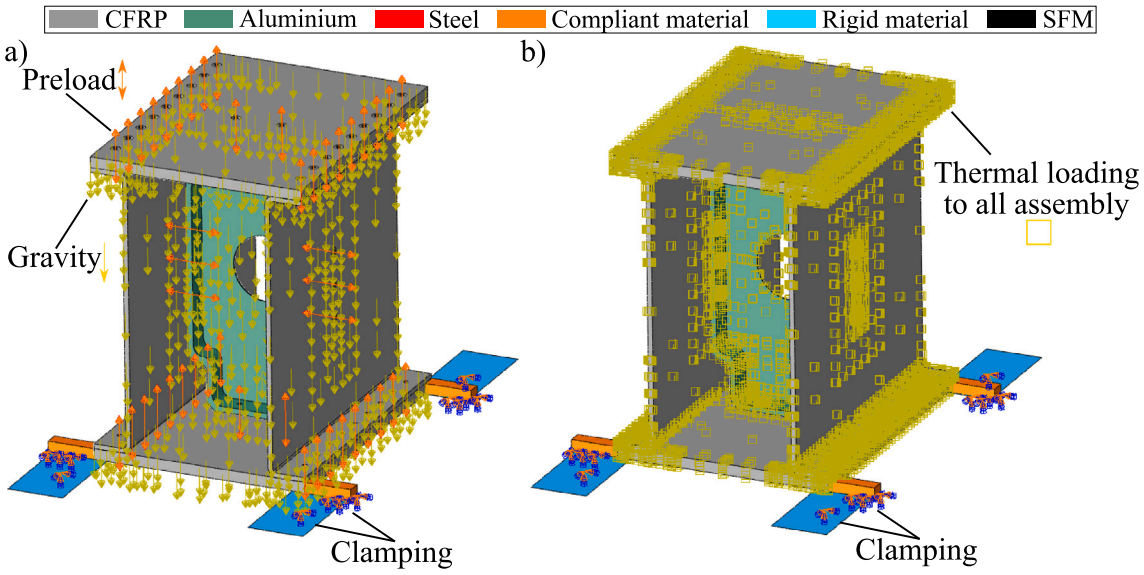

Fig. 8. Schema of the boundary conditions and steps used for the subcomponent finite element model. (a) Step 1 preload and (b) Step 2 thermal jump.

time and accuracy, and the use of typical elements available in Abaqus, makes the model feasible to be used by the industry to simulate large bolted structures, such as a Wingbox.

3. Results

Fig. 9, 10 and 11 present the location of the Strain Gauges (SG) along the rib, skin and spar, respectively, as well as the numerical predictions compared with the experimental values with a positive and negative thermal jump. In the rib, strain gauges SG1, SG2, SG3 and SG4 were placed around the central hole (to understand the deformation in such critical area) and at the top region of the rib, close to the connection with the skin (SG5–SG9), in an attempt to measure unfolding, see Fig. 9. Unfortunately, it was not possible to place strain gauges at the mouse hole since such an area is too small. In the skin, strain gauges SG1, SG2, SG3 and SG4 were placed close to the bolted joints with the rib at the centre, while SG5–SG8 were bonded next to the connection with the spar, and finally SG9 and SG10 were located close to the skin edge far away from any bolted joint. The strain gauges were bonded at the two surfaces of the skin (top and bottom) to understand the bending direction of the part by comparing the signals from both sides (such as, for instance, SG9 against SG10), see Fig. 10. Similarly, in the spar we placed strain gauges SG1–SG8 close to the three connections bolted with the rib, and SG9–SG12 far from any bolted joint. Moreover, strain gauges were again placed at each side of the spar (inner and outer) to assess the bending, see Fig. 11. Notice that, for the skin and spar, we also placed strain gauges in the longitudinal and transverse directions of the laminate.

The overall results show that the strains are compressive for the negative jump, and tensile for the positive thermal scenario. This indicates the components are under compression for the negative jump and expanding for the tensile one. In general, the model predicts reasonably well the magnitude of the strains as well as the sign and the trends with the rib, skin and spar. However, the model underpredicts the measurements in almost all locations. The longitudinal strains in the carbon parts are significantly lower than the rib, this is due to the large stiffness of the CFRP material and the low CTE in the fibre direction of the laminates (Table 3).

Fig. 12 shows the displacement magnitude of the structure with each thermal jump predicted by the FE model. Mainly, the rib experienced the highest contraction/expansion, thus forcing the skin and spar to bend. The deformed shape predicted by both thermal jumps are reversed one in respect to the other. With both thermal jumps the presence of unfolding between the rib and skin, and between the rib and spar can be noticed. This change in angle between the parts occurs due to the alteration in the primary shape of the ribs for which it was designed for. Unfolding can thus lead to an undesirable load carrying or stress distribution in the ribs in a manner it was not designed for, causing structural concerns. The rib design used in this work is therefore not able to prevent unfolding. Next, we analyse the deformed shape predicted between the model and experiments by comparing the strain gauge signals.

In the rib, SG1 and SG4 (both placed horizontally at each side of the central hole, see Fig. 9), give similar results with both thermal jumps, whereas SG2 (oriented vertically at the left of the hole) is lower in absolute terms than SG3 (also oriented vertically, but at the bottom of the hole). This indicates that the central hole is not deforming in a homogeneous manner, but rather into an elliptic shape. This is in line with the deformed shape in Fig. 12, and can be attributed to the fact that, the vertical deformation of the rib is more restricted by the presence of the skin, which is stiffer than the spar. In addition, SG5, SG6 and SG7 (placed vertically at the top region of the rib, see Fig. 9) are all quite similar. Consequently, the top region of the rib deforms in a homogeneous way, this is again consistent with Fig. 12. However, we note that, while unfolding between the rib and skin is clearly happening in the numerical model, the strain magnitudes from the top of the rib are not able to indicate the presence of this phenomenon, neither in the simulation nor the experiments. Therefore, to properly corroborate the unfolding phenomenon (which is captured in the model) with the experimental strain measurements, strain gauges need to be placed at appropriate locations which will need further investigation. Further, SG10 coincides with SG8, indicating symmetry with respect to the horizontal axis.

In the skin, for the positive thermal case, SG1, which is placed transversally at the centre of the top surface just at the connection with the rib, is larger (in absolute terms) than SG4, placed at the same location but at the bottom surface, see Fig. 10. A similar observation can be made between SG2 and SG3, placed at the same areas but in the longitudinal direction. Hence, these differences between the strain signals at the top and bottom surfaces indicate that the skin is bending upwards (away from the rib), because it is being pushed by the expanding rib. This is again in line with the deformed shape in Fig. 12. The negative thermal case should follow the opposite trend, however SG3 and SG4 failed during the experimental test.

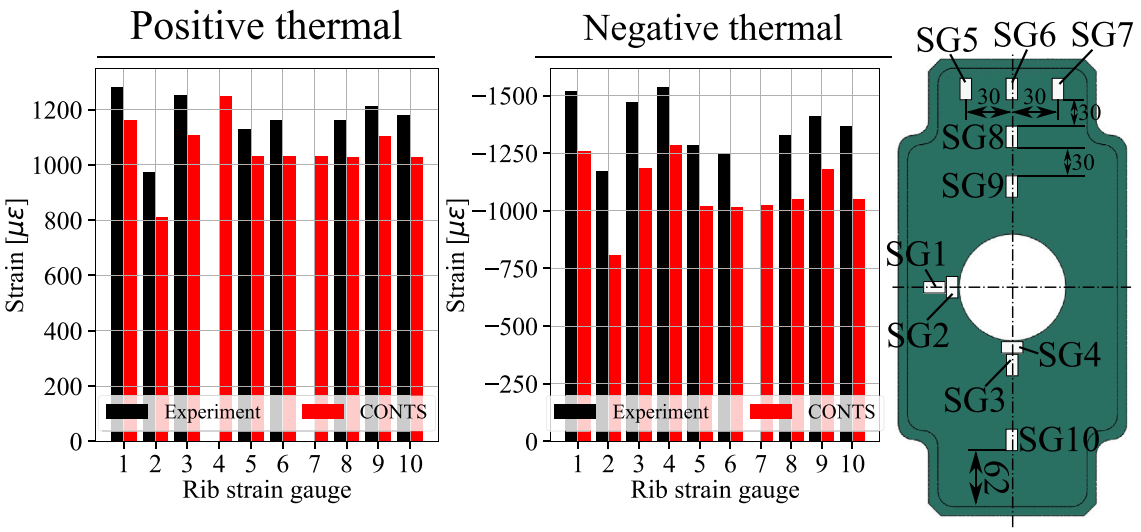

Fig. 9. Location of the strain gauges in the rib and comparison of the experimental strain gauge measurements against the numerical results for positive and negative thermal jumps. The SG4 with positive thermal and SG7 (for both tests) are not shown since they failed during the test.

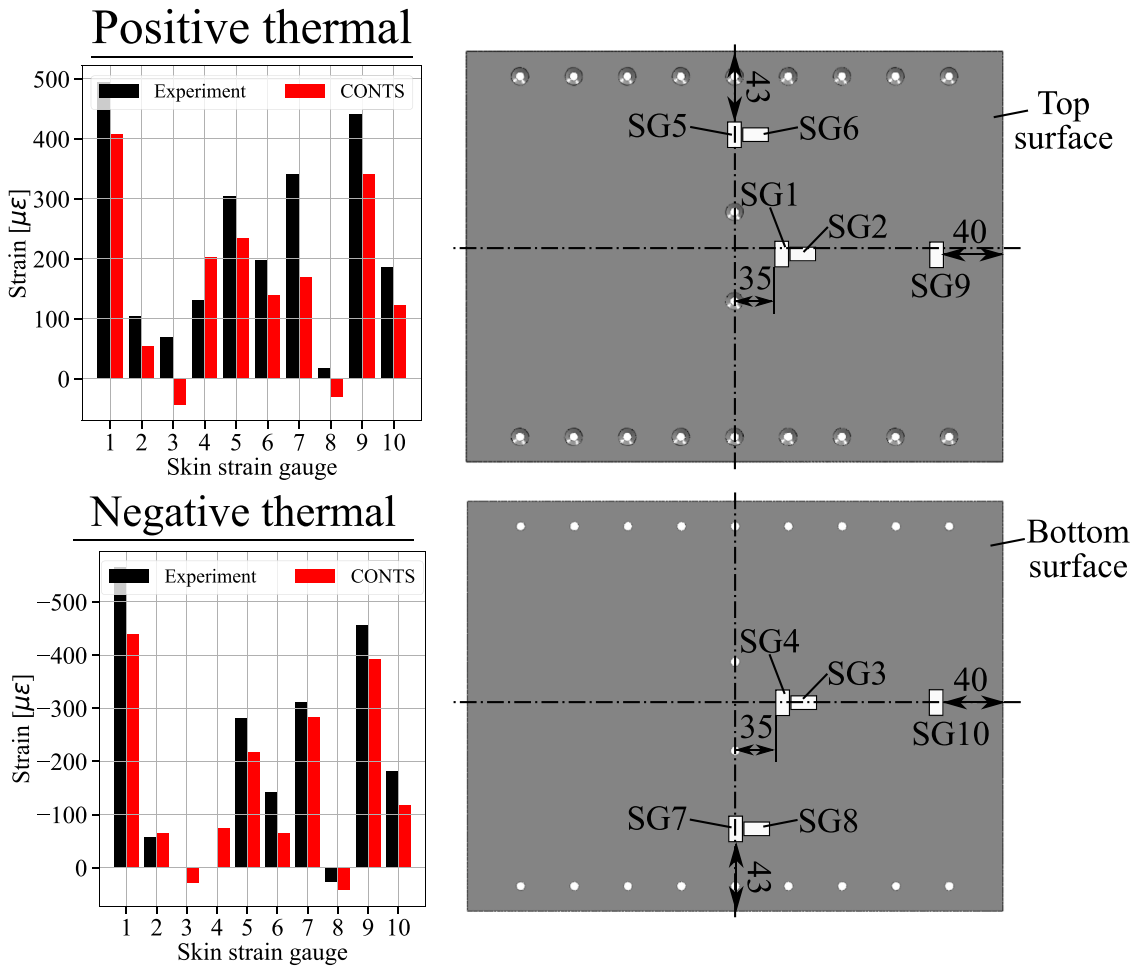

Fig. 10. Location of the strain gauges in the top skin and comparison of the experimental strain gauge measurements against the numerical results for positive and negative thermal jumps. The SG3 with the negative thermal is not shown since it failed during the test.

In the negative test, SG8, placed longitudinally next to the connection with the spar, shows tensile strains, whereas SG6 (located at the same place, but at the bottom surface) exhibits compressive strain. The positive test shows the reversed trend. Hence, this indicates again that the skin bends upwards, pushed by the rib when the thermal jump is positive, whereas the opposite occurs with the negative thermal. The transverse strain gauges placed in that location, SG5 and SG7, show the same trends for the negative thermal. Nonetheless, for the positive thermal although the CONTS predicts that SG5 is larger than SG7, the experiments show the opposite. The strain gauge placed near the

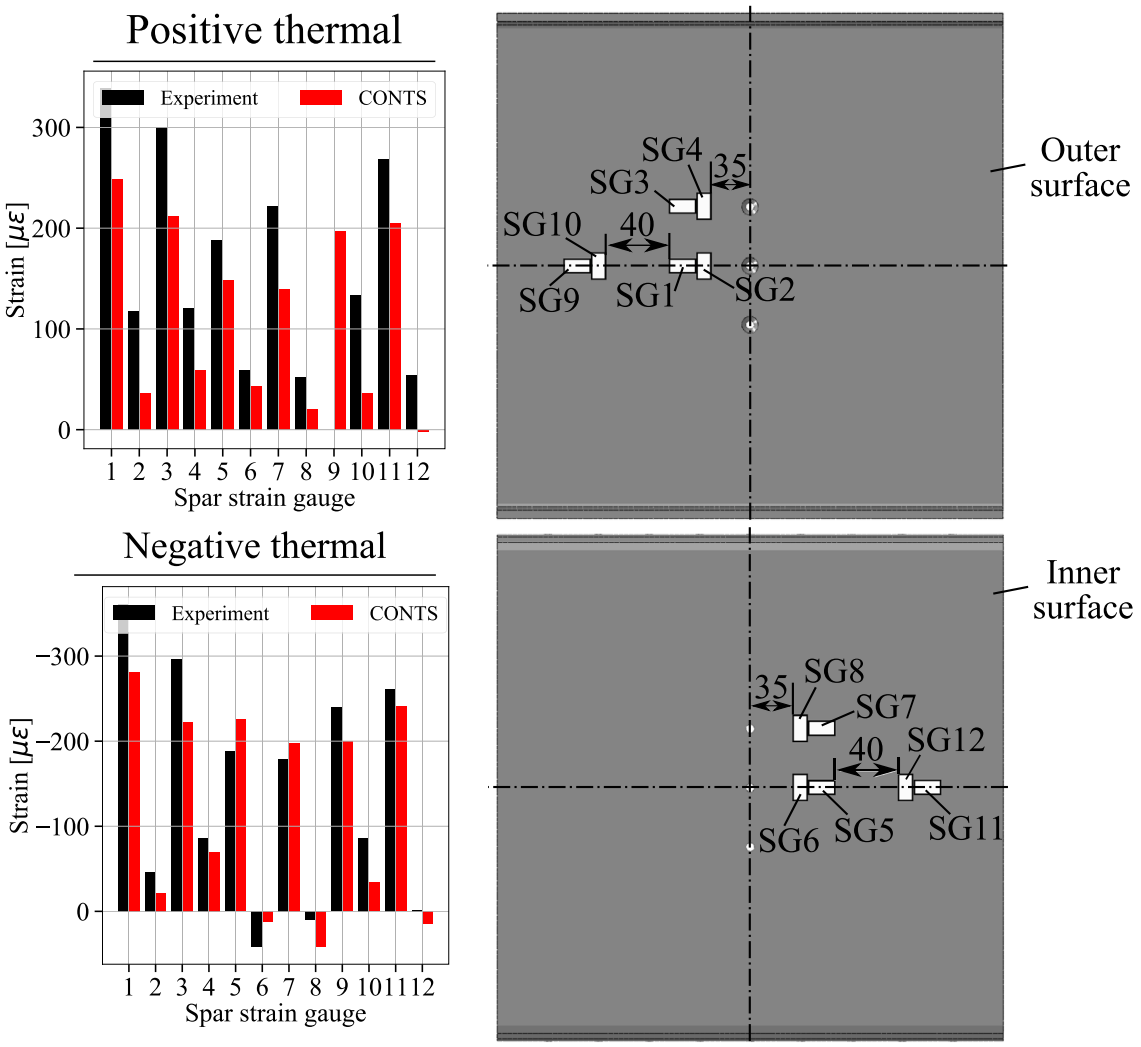

Fig. 11. Location of the strain gauges in the left spar and comparison of the experimental strain gauge measurements against the numerical results for positive and negative thermal jumps. The SG9 with the positive thermal is not shown since it failed during the test.

edge of the skin and far from any bolted connection, SG10, presents lower absolute strain than SG9 (located at the same place, but at the top surface), this indicates again the same kind of deformed shape discussed, but with a smaller relative difference between both of them. Hence, there is less bending far from the centre of the skin (Fig. 12).

For the spar, with both thermal jumps, SG1, longitudinally placed next to the central bolted joint with the rib, is larger (in absolute terms) than SG5, which is located at the same place but at the inner surface. Similarly, in the transversal direction, SG2 is also larger than SG6, see Fig. 11. This implies the spar is bending outwards, as it is being pushed by the expanding rib (for the positive thermal case), while it is bending inwards (being pulled by the compressing rib) under the negative thermal. This, once again, agrees well with the deformation of the FE model seen in Fig. 12. The same observation can be made by comparing SG3 to SG7 and SG4 to SG8, which were placed close to the upper bolted joint with the rib. In addition, SG10, located transversally close to the spar edge and far from the bolted joints, also shows higher absolute strains than SG12 (in the same place, but at the inner surface), leading to the same deformed shape explained. The relative difference between both magnitudes is still significant compared to the other strain gauges placed towards the bolted joints, which indicates the spar is still bent far from the connection to the rib (Fig. 12).

The good agreement between the numerical and experimental predictions instil confidence in the modelling and experimental approaches. Next, we use the FE model to provide more insight into the global behaviour and the critical areas of the substructure, which cannot be done easily with experimental testing.

Fig. 13 shows the Von Mises stress for the positive and negative thermal jumps in the rib, whereas Fig. 14 presents the stress in the fibre direction (S11), in the matrix direction (S22) and the in-plane shear stress (S12) in the laminates. The skin shows the maximum stresses at the connection with the rib, caused by the large CTE mismatch between the parts that attempted to expand or contract differently. Likewise, the most critical areas in the spar are also the bolted joints with the rib. In any case, the stress levels in the laminates are too small to be of concern, since even the maximum stress values are very low compared with the typical strengths of similar aeronautical materials [36]. On the other hand, the rib presents much higher stress levels relative to the strength and yield stress of these kind of aluminium alloys (in this case Aluminium 2024-O). Therefore, the rib is the most critical element in the thermal response of this wingbox subcomponent assembly. The main areas of concern in the rib are clearly observed: the central hole of the rib, the rib mouse hole and the bolted joints. Next, we analyse these critical regions in detail.

The hoop stresses in the central hole of the rib are presented in Fig. 15. In the positive thermal scenario, tensile hoop stresses of about 15 MPa appear at the top and bottom of the hole, while compressive stresses of about 30 MPa appear to the left and right sides. On the other hand, the negative thermal case shows up to 50 MPa tensile stresses to the left and side of the hole, and up to 16 MPa compressive stresses

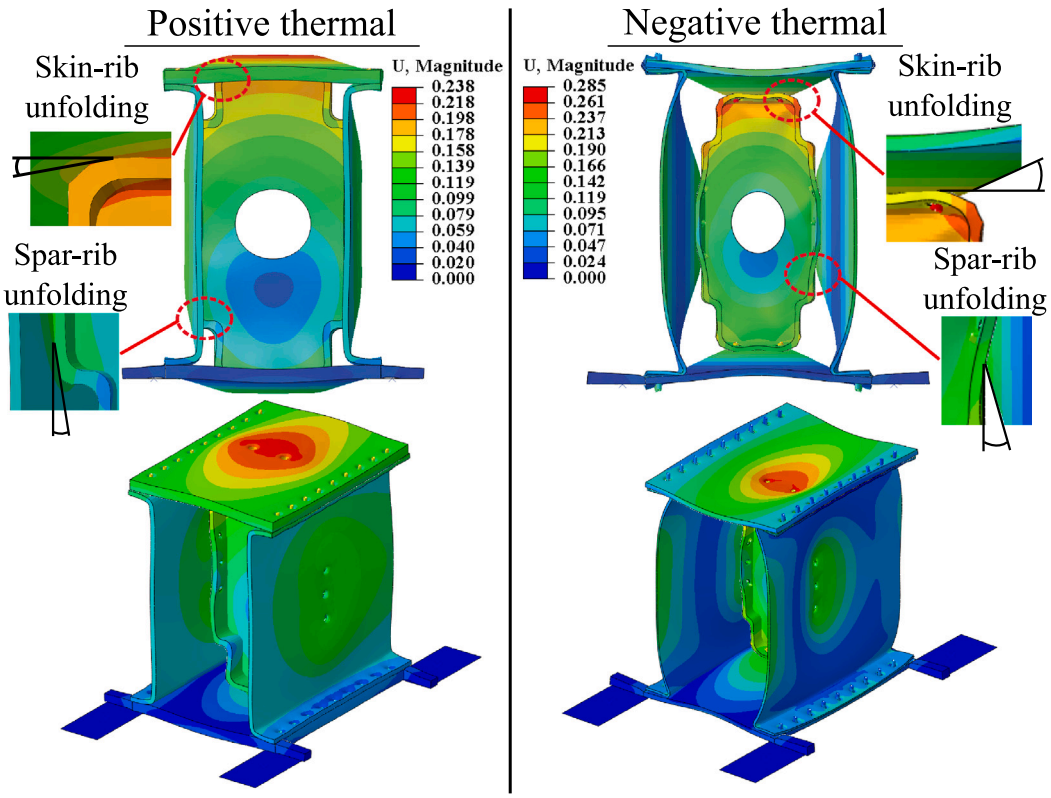

Fig. 12. Displacement magnitude predicted by the numerical model with both thermal jumps (positive and negative). The deformation scale factor is 150.

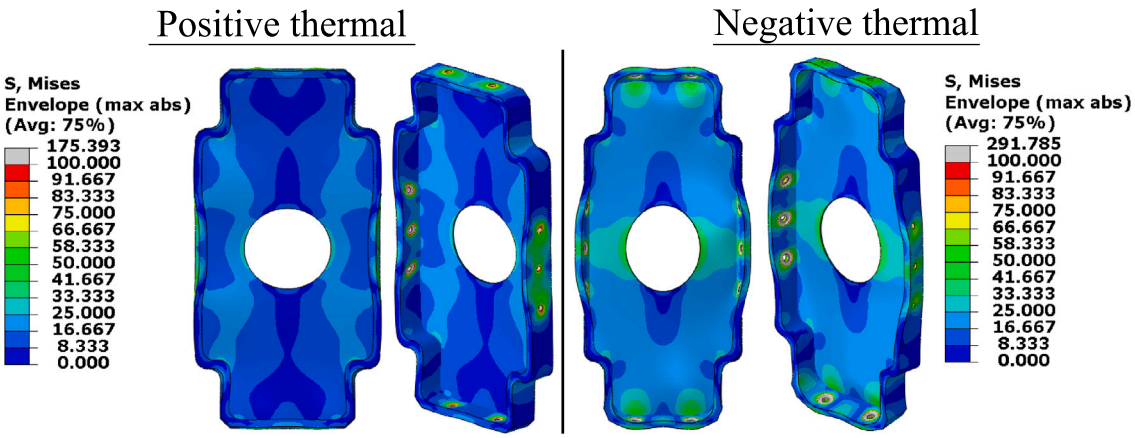

Fig. 13. Von Mises stress predicted by the FE model with both thermal jumps (positive and negative) in the rib. The deformation scale factor is 150.

at the top and bottom of the hole. Thus, for both loading scenarios the areas under tension and compression are reversed. This is the reason for the different elliptical shapes in positive and negative jumps. In both cases, the tensile hoop stresses become a significant concern, since only a pure thermal step can create tensile hoop stresses of up to 50 MPa at the central hole of the rib. The subsequent repetition of this thermal cycle on the assembly could easily trigger the nucleation of a crack that could eventually grow with the increase in the thermal fatigue cycles. In addition, for a real wingbox structure, the authors presume the magnitude of these hoop stresses can increase significantly for rib bays that are far away from the spar connections. Notice these trends agree well with the strain signals shown in Fig. 9: with the positive thermal, SG4 (bottom of hole) is more tensile than SG2 (left of hole), while with the negative thermal, SG4 is more compressive than SG2.

The hoop stresses in the rib mouse hole are presented in Fig. 16. Under positive thermal, tensile stresses appear in the inner side of the mouse hole, whereas compressive stresses occur on the outside. The reverse is seen with the negative thermal. The tensile stresses are again larger with the negative thermal case. As in the central hole, these tensile hoop stresses may be critical during fatigue cycles.

The change in the longitudinal stress in some of the bolts, due to the thermal loading, is presented in Fig. 17. This stress is computed as the clamping load divided by the bolt's cross-sectional area. Under the positive thermal, the bolts suffer an increase of longitudinal stress due to the higher expansion of the bolted components that are forcing the bolt to increase its length. This is considered to be critical as the bolt stress may exceed the yield stress and deform plastically. The opposite phenomenon occurs with the negative thermal, which, in some cases, could lead to the separation of the joint if the preload is fully lost [7]. This proves also that changes in bolt stress or preload need to be taken into account in the design of a wingbox [7]. The most critical bolts are

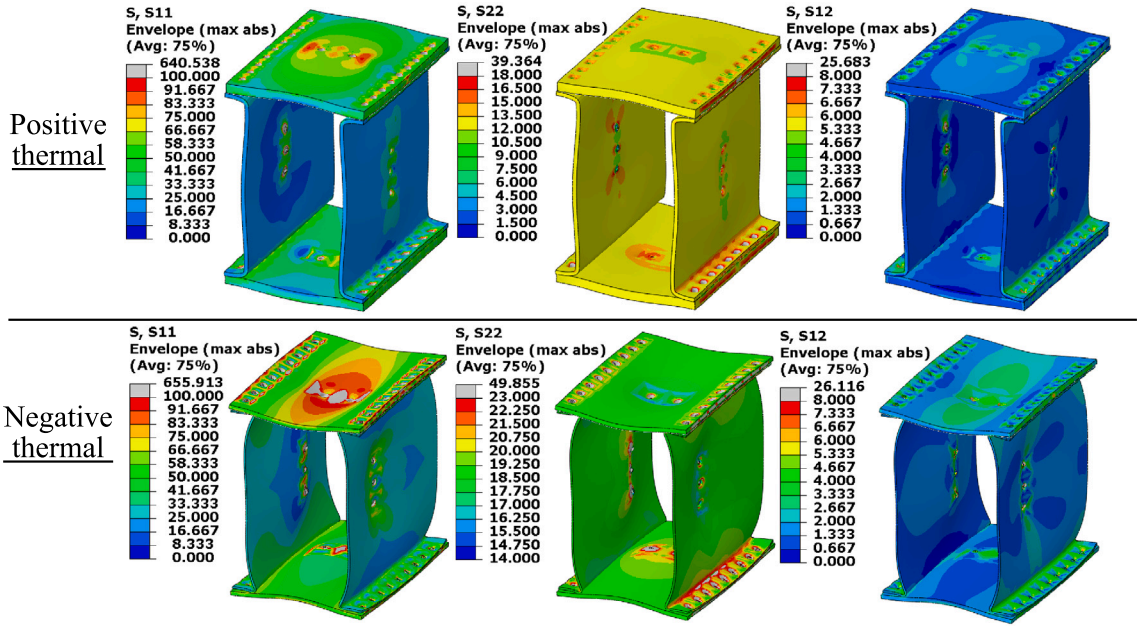

Fig. 14. Stress in the fibre direction (S11), in the matrix direction (S22) and the in-plane shear (S12) stress predicted by the FE model with both thermal jumps (positive and negative) in the laminates. The deformation scale factor is 150. The maximum stress across all plies contained by each element through the thickness is shown.

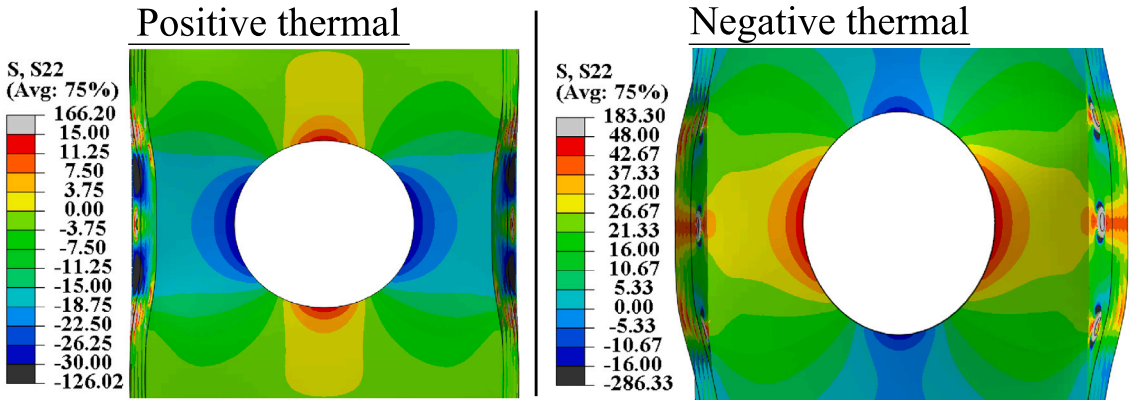

Fig. 15. Numerical prediction of the hoop stresses around the central hole in the rib with positive and negative thermal jump. The deformation scale factor is 150.

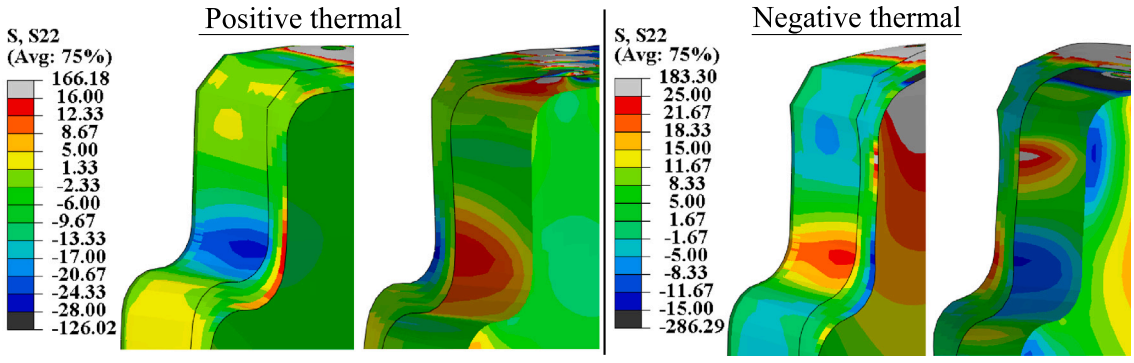

Fig. 16. Numerical prediction of the hoop stresses around the mouse hole in the rib with positive and negative thermal jump. The deformation scale factor is 150.

those bolting the skin and rib, since this is the area with higher bending stress (Figs. 12 and 14).

Finally, the computational time using 24 cpus, was 3 h and 14 min for the negative thermal simulation, and 2 h and 59 min for the positive one.

4. Discussion

The previous section has presented the experimental results obtained on a wingbox subcomponent and has validated an FE model previously developed in Guerrero et al. [7].

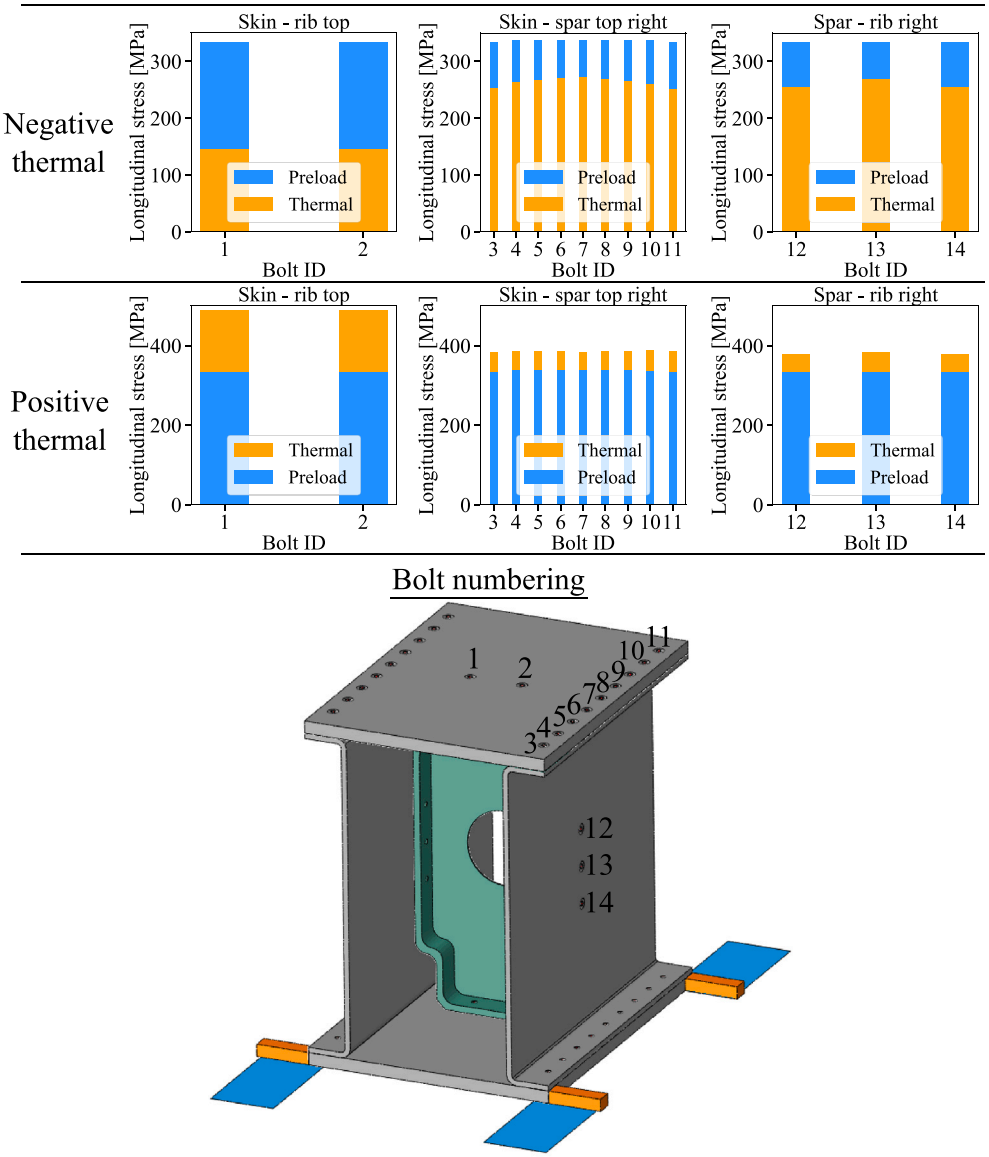

Fig. 17. Numerical prediction of the longitudinal stress in some bolts with positive and negative thermal jump.

The results prove that the FE model used to simulate a carbon–aluminium hybrid wingbox substructure with 46 bolts subjected to thermal effects, is rich enough to capture the response of a real structure, while still being computationally efficient. The fact that the trends of the model correlated well with the experimental data proves that the numerical deformed shape predicted is correct and in line with the experiments. Consequently, the use of beam and surface elements is accurate enough to capture the presence of the bolts. The disadvantage of beams is that they may fail to accurately capture the stresses in the bolts [3]. Nonetheless, this issue can be solved by means of submodelling, where the beam could be replaced by a 3D solid. Alternatively, 3D solid bolts could be used instead of beams in the most critical locations. Further to this, the agreement indicates that omitting the washer and nut has little impact on the global predictions [7].

Results indicate that the rib is the critical structural element in the thermal response of a wingbox substructure [7]. Due to the larger CTE of the aluminium, the rib tries to expand or contract more than the skin, spar and bolts, and hence, either pushes or pulls them accordingly (see Fig. 12, 13 and 14). However, the deformation is clearly not homogeneous at all. This is proven by the signals of SG1 and SG4 in the rib, which are higher than SG2 and SG3. While the horizontal deformation of the rib is constrained by the spar, the vertical deformation is constrained by the skin. Since the skin is stiffer than the spar, there is less rib deformation in the vertical direction. This can also be observed with SG8 and SG9, whose values are much higher than SG5, SG6 and SG7 placed close to the skin. In addition, both thermal jumps induce high hoop stresses especially in the negative thermal case. These stresses can potentially trigger a fatigue crack if not carefully analysed. The thermal loads can also cause bolt yielding and loss of bolt preload. Therefore, the bolt preload should be selected carefully to avoid yielding in the positive thermal and loosening in the negative thermal case. Further to this, the numerical model shows that this kind of rib design cannot prevent the presence of unfolding. Unfortunately, it was not possible to monitor this phenomenon during the experimental testing to validate the model prediction.

Recall, nonetheless, that the subcomponent represents just a small unit of a full wingbox, see Fig. 1. It is therefore arguable whether a single rib unit is a good representation of a full wingbox that contains several rib bays. Indeed, the rib bays placed towards the middle of a full wingbox may behave differently than the bays placed to the sides in the connection with the spars (Fig. 1). This might not be represented by a single-bay subcomponent. Hence, although the subcomponent can

serve as a preliminary design tool, it may not be fully representative of a full wingbox assembly. Whether the subcomponent is actually representative or not will be assessed in future work.

The numerical model shows a constant underprediction of the strain compared against the experimental tests, see Fig. 9, 10 and 11. There are several explanations for this discrepancy, which are discussed as follows.

- Composite laminates can have residual stresses coming from the curing cool-down process [37]. These residual stresses can easily be estimated, however, additional residual stresses occur during the assembly of the parts. It is difficult, if not impossible, to account for these stresses in the simulation of a large structure.
- In the experiments, the temperature is not perfectly uniform and thermal gradients along the different regions of the assembly occur (Fig. 2). In the numerical simulations, the stabilised temperature at the end of the tests is applied uniformly. The difference between this temperature and the real one can lead to some discrepancy especially when comparing very low strains like in the CFRP laminates.
- The strain gauge signals found in the laminated parts (skin and spar, see Figs. 10 and 11) are comparatively small, and thus the strain gauges may fail to capture such low magnitudes accurately. Furthermore, the strain signals from the experiments were corrected by using Eq. (2). However, the strain due to the strain gauge resistance change, ε_p, which is calculated from the datasheet, has some uncertainty associated (see Table 1). Given that the strains are so small, even small deviations in the correction of the strain signals could lead to large errors.
- The CTEs measured on the CFRP laminate showed significant scatter in the fibre direction (α_{11}, see Table 3). It is important to highlight that α_{11} significantly affects the equivalent CTE of the laminate computed by classical laminate theory. Hence, small deviations in the CTE can cause large errors.

Considering all the possible issues and the relative simplicity of the model, the agreement between the numerical model and the experiment is remarkable. Indeed, from a total of 32 strain gauges, the biggest discrepancy between the model and experiments occurs with SG3 and SG8 in the skin under the positive thermal, which are predicted as negative in the simulations, but positive in the experiments. However, the values in these strain gauges are close to zero and, considering the issues stated, the differences overall are not important. The experimental methodology carried out has also proved to be good enough to capture the main response of the structure and engender confidence in the numerical model. Nonetheless, it is worth mentioning that the present work has focused on the thermal response of a subcomponent of a wingbox, without taking into account mechanical loads. In reality, the wingbox will be subjected to a combination of thermal and mechanical loads, hence, compromising further the integrity of the assembly. Finally, we recall again the efficiency of the FE approach, since in only three hours of computational time, we are able to simulate the subcomponent comprising of 46 bolted joints with more than half a million elements.

5. Conclusions

Aircraft manufacturers are currently concerned about the behaviour of bolted joint assemblies between dissimilar materials under thermal loading, due to the mismatch thermal expansion of the parts that induces significant thermal stresses. This work has studied the behaviour of a hybrid substructure assembly experimentally and numerically.

On the one hand, a hybrid carbon–aluminium wingbox subcomponent with 46 bolts was manufactured and tested under transient thermal loading conditions. The subcomponent was instrumented with strain gauges to capture the global deformation of the assembly. A simple approach was proposed and validated to correct the strain gauge measurements from the experiments, due to the thermal output of the strain gauges. On the other hand, by using an FE model based on continuum shells to represent the bolted plates, beam elements and SFM to model the bolts, as well as multi-point constraints to model the washer and nut, we have been able to simulate the relatively complex wingbox subcomponent assembly with little computational effort. The model accounts for all relevant phenomenology (contacts and frictional sliding, bolt preload, bolt-hole clearance, thermal expansion or contraction and simplified through-thickness behaviour). The results of the experimental tests were compared with the numerical simulation.

Results show that the strain predictions given by the FE model compare reasonably well with the experimental data. Not only were the metallic components (rib) well predicted, but likewise the composite laminates (skin and spar) were in excellent agreement. In addition, the deformed shape predictions between the model and experiments were in line with each other. The results prove that the rib is the main driving mechanism during the thermal expansion or contraction of a hybrid wingbox, due to the increased thermal expansion coefficient compared with the CFRP skins and spars. When the assembly is heated or cooled down, the rib either expands or contracts and pushes the skin and spar to bend accordingly, leading to stresses in the assembly. Even though the temperature jumps were reasonably small, significant stresses appeared, which may trigger damage during cyclic loading. Hence, thermal loadings should be taken into account during the design process. Due to the model's accuracy, we claim that the approach proposed can be used as virtual testing and replace the complex and expensive experimental campaign. Our experimental methodology has also been proved to be accurate. In addition, we provided insight into the importance of the strain gauge selection and the strain correction for pure thermal cases.

Future work will use the same experimental methodology to test a full one-meter-long hybrid wingbox assembly with several hundreds of bolts, and use the same numerical approach to reproduce the experimental test.

CRediT authorship contribution statement

José M. Guerrero: Conceptualization, Methodology, Validation, Formal analysis, Investigation, Writing – original draft, Writing – review & editing. **Aravind Sasikumar:** Conceptualization, Methodology, Validation, Formal analysis, Investigation, Writing – review & editing. **Jordi Llobet:** Conceptualization, Methodology, Validation, Formal analysis, Investigation, Writing – review & editing. **Josep Costa:** Conceptualization, Methodology, Validation, Formal analysis, Investigation, Writing – review & editing, Supervision.

Declaration of competing interest

The authors declare that they have no known competing financial interests or personal relationships that could have appeared to influence the work reported in this paper.

Data availability

The raw/processed data required to reproduce these findings cannot be shared at this time due to legal and/or ethical reasons.

Acknowledgements

This work was carried out under the framework of the EU H2020 Clean Sky 2 Project INNOHYBOX - Innovative solutions for metallic ribs or fittings introduced in a composite box to optimally deal with thermo-mechanical effects. This project has received funding from the Clean Sky 2 Joint Undertaking (JU) under grant agreement No. 785433. The JU receives support from the European Union's Horizon 2020 research and innovation programme and the Clean Sky 2 JU members other than the European Union.

References

[1] Kapidžić Z, Nilsson L, Ansell H. Conceptual studies of a composite-aluminum hybrid wing box demonstrator. Aerosp Sci Technol 2014;32(1):42–50. http://dx.doi.org/10.1016/j.ast.2013.11.002.

[2] Sasikumar A, Guerrero JM, Quintanas-Corominas A, Costa J. Numerical study to understand thermo-mechanical effects on a composite- aluminium hybrid bolted joint. Compos Struct 2021;275:114396. http://dx.doi.org/10.1016/j.compstruct.2021.114396.

[3] Stocchi C, Robinson P, Pinho ST. A detailed finite element investigation of composite bolted joints with countersunk fasteners. Composites A 2013;52:143–50. http://dx.doi.org/10.1016/j.compositesa.2012.09.013.

[4] Omran O, Nguyen VD, Jaffal H, Coorevits P. Development of a connector element for multi-material bolted-joint under tensile loading. Mech Adv Mater Struct 2018;1–12. http://dx.doi.org/10.1080/15376494.2018.1452314.

[5] Hirano NY, Takao Y, Wang WX. Effects of temperature on the bearing strength of CF/epoxy pinned joints. J Compos Mater 2007;41(3):335–51. http://dx.doi.org/10.1177/0021998306063374.

[6] Coman CD, Constantinescu DM. Temperature effects on joint strength and failure modes of hybrid aluminum–composite countersunk bolted joints. Proc Inst Mech Eng Part L: J Mater: Design Appl 2019;233(11):2204–18. http://dx.doi.org/10.1177/1464420719837299.

[7] Guerrero JM, Sasikumar A, Llobet J, Costa J. A computationally efficient methodology to simulate hybrid bolted joints including thermal effects. Mech Adv Mater Struct 2022;1–19. http://dx.doi.org/10.1080/15376494.2021.2007555.

[8] Madenci E, Shkarayev S, Sergeev B, Oplinger DW, Shyprykevich P. Analysis of composite laminates with multiple fasteners. Int J Solids Struct 1998;35(15):1793–811. http://dx.doi.org/10.1016/S0020-7683(97)00152-2.

[9] McCarthy MA, Lawlor VP, Stanley WF, McCarthy CT. Bolt-hole clearance effects and strength criteria in single-bolt, single-lap, composite bolted joints. Compos Sci Technol 2002;62(10–11):1415–31. http://dx.doi.org/10.1016/S0266-3538(02)00088-X.

[10] Girard C, Dano ML, Picard A, Gendron G. Bearing behavior of mechanically fastened joints in composite laminates - part I: Strength and local strains. Mech Adv Mater Struct 2003;10(1):1–21. http://dx.doi.org/10.1080/15376490390118102.

[11] Zhao L, Fang Z, Liu F, Shan M, Zhang J. A modified stiffness method considering effects of hole tensile deformation on bolt load distribution in multi-bolt composite joints. Composites B 2019;171:264–71. http://dx.doi.org/10.1016/j.compositesb.2019.05.010.

[12] EASA. Notification of a proposal to issue an airworthiness directive: Wing rib feet modification.

[13] Airbus. A380 wing flaw undetected for a decade. https://www.reuters.com/article/uk-airbus-a380/airbus-a380-wing-flaw-undetected-for-a-decade-idUKLNE84O00J20120525.

[14] Rouchon J. Certification of large airplane composite structures, recent progress and new trends in compliance philosophy. 1990.

[15] Jumbo FS, Ashcroft IA, Crocombe AD, Abdel Wahab MM. Thermal residual stress analysis of epoxy bi-material laminates and bonded joints. Int J Adhes Adhes 2010;30(7):523–38. http://dx.doi.org/10.1016/j.ijadhadh.2010.03.009.

[16] Skrna-Jakl IC, Stiftinger MA, Rammerstorfer FG. Numerical investigations of an imperfect stringer-stiffened composite wing torsion box - an analysis concept. Composites B 1996;27(1):59–69. http://dx.doi.org/10.1016/1359-8368(95)00007-0.

[17] Ireman T. Three-dimensional stress analysis of bolted single-lap composite joints. Compos Struct 1998;43(3):195–216. http://dx.doi.org/10.1016/S0263-8223(98)00103-2.

[18] Tserpes KI, Labeas G, Papanikos P, Kermanidis T. Strength prediction of bolted joints in graphite/epoxy composite laminates. Composites B 2002;33(7):521–9. http://dx.doi.org/10.1016/S1359-8368(02)00033-1.

[19] McCarthy MA, McCarthy CT, Lawlor VP, Stanley WF. Three-dimensional finite element analysis of single-bolt, single-lap composite bolted joints: Part I - Model development and validation. Compos Struct 2005;71(2):140–58. http://dx.doi.org/10.1016/j.compstruct.2004.09.024.

[20] McCarthy CT, McCarthy MA. Three-dimensional finite element analysis of single-bolt, single-lap composite bolted joints: Part II - effects of bolt-hole clearance. Compos Struct 2005;71(2):159–75. http://dx.doi.org/10.1016/j.compstruct.2004.09.023.

[21] McCarthy CT, McCarthy MA, Lawlor VP. Progressive damage analysis of multi-bolt composite joints with variable bolt-hole clearances. Composites B 2005;36(4):290–305. http://dx.doi.org/10.1016/j.compositesb.2004.11.003.

[22] Egan B, McCarthy CT, McCarthy MA, Gray PJ, Frizzell RM. Modelling a single-bolt countersunk composite joint using implicit and explicit finite element analysis. Comput Mater Sci 2012;64:203–8. http://dx.doi.org/10.1016/j.commatsci.2012.02.008.

[23] Zhou Y, Yazdani-Nezhad H, McCarthy MA, Wan X, McCarthy C. A study of intra-laminar damage in double-lap, multi-bolt, composite joints with variable clearance using continuum damage mechanics. Compos Struct 2014;116(1):441–52. http://dx.doi.org/10.1016/j.compstruct.2014.05.051.

[24] Mandal B, Chakrabarti A. A simple homogenization scheme for 3D finite element analysis of composite bolted joints. Compos Struct 2015;120:1–9. http://dx.doi.org/10.1016/j.compstruct.2014.09.061.

[25] Mandal B, Chakrabarti A. Numerical failure assessment of multi-bolt FRP composite joints with varying sizes and preloads of bolts. Compos Struct 2018;187(2017):169–78. http://dx.doi.org/10.1016/j.compstruct.2017.12.048.

[26] Gray PJ, McCarthy CT. A highly efficient user-defined finite element for load distribution analysis of large-scale bolted composite structures. Compos Sci Technol 2011;71(12):1517–27. http://dx.doi.org/10.1016/j.compscitech.2011.06.011.

[27] Richards WL. A new correction technique for strain-gage measurements acquired in transient-temperature environments, Vol. 3593. NASA technical paper, 1996.

[28] Micro-measurements. Strain gage thermal output and gage factor variation with temperature. In: Tech note TN-504-1, Vol. 11054. 2014.

[29] ASTM standard E228-11. Standard test method for linear thermal expansion of solid materials with a push-rod dilatometer. ASTM Int 2011.

[30] Dassault Systemes/ SIMULIA. ABAQUS version 6.14 documentation. ABAQUS, Inc.; 2014.

[31] DiNicola A, Fantle S. Bearing strength behavior of clearance-fit fastener holes in toughened graphite/epoxy laminates. In: Eleventh volume: composite materials—testing and design. 1993, p. 220–37. http://dx.doi.org/10.1520/STP12630S.

[32] ASTM D3039 / D3039M-17. Standard test method for tensile properties of polymer matrix composite materials. ASTM Int 2017. www.astm.org.

[33] ASTM D3518 / D3518M-18. Standard test method for in-plane shear response of polymer matrix composite materials by tensile test of a ±45° laminate. ASTM Int 2018. www.astm.org.

[34] MatWeb. Material property data. 2011, http://www.matweb.com/.

[35] Kim J, Yoon JC, Kang BS. Finite element analysis and modeling of structure with bolted joints. Appl Math Model 2007;31(5):895–911. http://dx.doi.org/10.1016/j.apm.2006.03.020.

[36] Llobet J, Maimí P, Turon A, Bak BL, Lindgaard E, Carreras L, et al. A continuum damage model for composite laminates: Part IV- experimental and numerical tests. Mech Mater 2021;154(2020):103686. http://dx.doi.org/10.1016/j.mechmat.2020.103686.

[37] Swolfs Y, Gorbatikh L, Verpoest I. Fibre hybridisation in polymer composites: A review. Composites A 2014;67:181–200. http://dx.doi.org/10.1016/j.compositesa.2014.08.027.